journal of the mechanical behavior of biomedical materials 139 (2023) 105690

Contents lists available at ScienceDirect

Journal of the Mechanical Behavior of Biomedical Materials

journal homepage: www.elsevier.com/locate/jmbbm

Research paper

Modelling and validation of the non-linear elastic stress–strain behaviour of multi-layer silicone composites

Mohammad Ahmad [a], Xavier Pelorson [a], Oriol Guasch [b], Ana Inés Fernández [c], Annemie Van Hirtum [a,*]

[a] Univ. Grenoble Alpes, CNRS, Grenoble INP, LEGI, 38000 Grenoble, France
[b] Department of Engineering, La Salle, Universitat Ramon Llull, Spain
[c] Department of Materials Science and Physical Chemistry, University of Barcelona, Spain

ARTICLE INFO

Keywords:
Non-linear stress–strain model
Effective low-strain and high-strain Young's modulus
Phenomenological model
Silicone composites
Mechanical vocal fold replica

ABSTRACT

Multi-layer silicone composites are commonly used to mold deformable silicone vocal folds replicas. Nevertheless, so far the stress–strain characterisation of such composite specimens is limited to their effective Young's modulus (up to 40 kPa) characterising the elastic low-strain range, *i.e.* up to about 0.3. Therefore, in this work, the characterisation is extended to account for the non-linear strain range. Stress–strain curves on 6 single-layer and 34 multi-layer silicone specimens, with different layer stacking (serial, parallel, combined or arbitrary), are measured at room temperature using uni-axial tensile tests for strains up to 1.36, which amounts to about 4.5 times the extent of the linear low-strain range. Cubic polynomial and exponential two-parameter relationships are shown to provide accurate continuous fits (coefficient of determination $R^2 \geq 99\%$) of the measured stress–strain data. It is then shown that the parameters can be *a priori* modelled as a constant or as a linear function of the effective low-strain Young's modulus for strains up to 1.55, *i.e.* 5 times the low-strain range. These *a priori* modelled parameter are confirmed by approximations of the best fit parameters for all assessed specimens as a function of the low-strain Young's modulus. Thus, the continuous stress–strain behaviour up to 1.55 can be predicted analytically from the effective low-strain Young's modulus either using the modelled parameters ($R^2 \geq 85\%$) or the approximations of the best fit parameter sets ($R^2 \geq 94\%$). Accurate stress–strain predictions are particularly useful for the design of composites with different composition and stacking. In addition, analytical expressions of the linear high-strain Young's modulus and the linear high-strain onset, again as a function of the effective low-strain Young's modulus, are formulated as well.

1. Introduction

Human voice production is due to the auto-oscillation of the vocal folds following the fluid–structure interaction (FSI) between the airflow coming from the lungs and the surrounding vocal folds tissue. Since 2008 (Riede et al., 2008; Drechsel and Thomson, 2008), physical studies of this fluid–structure interaction (FSI) often rely on deformable molded multi-layer (ML) composite silicone vocal fold (VF) replicas. Their usage is mainly motivated by the possibility to mimick – up to some degree – the (micro-)anatomical ML representation of the human VF structure, which consists of overlapping muscle (Mu), vocal ligament (Li), superficial (Su) and cover epithelium (Ep) layers (Rosen and Simpson, 2008). Elastomer silicone mixtures (either Thinner-Ecoflex (TE) or Thinner-Dragonskin (TD)) at different mass mixing ratios $\mathcal{M} = r_T : r_{E(D)}$ (with constant $r_{E(D)} = 2$) allow to vary the low-strain elastic Young's modulus $\mathcal{E}$ of individual layers in order to match the range reported for human VF layers, *i.e.* 8–29 kPa for Mu, 10–45 kPa for Li, 2–9 kPa for Su and 40–60 kPa for Ep (Hirano et al., 1983; Alipour and Titze, 1991; Min et al., 1995; Chan et al., 2007; Chhetri et al., 2011; Smith and Thomson, 2012; Miri, 2014; Zhang et al., 2017). Commonly used silicone mixtures (I_n, $n = 1 \ldots 6$) are summarised in Table 1. Mixtures I_1 up to I_5 (with $2 \leq \mathcal{E} \leq 65$ kPa) are used to mold the two-layer M5 replica (Mu and Su with I_3 and I_2 (Pickup and Thomson, 2010)), the three-layer MRI replica (Mu, Su and Ep with I_2, I_1 and I_5 (Pickup and Thomson, 2010; Bouvet et al., 2020a,b)) and the four-layer EPI replica (Mu, Li, Su and Ep with I_4, I_2, I_1 and I_5 (Murray and Thomson, 2012; Bouvet et al., 2020a,b)). An additional mixture I_6 with greater low-strain Young's modulus so that $4 \leq \mathcal{E}_{I_6}/\mathcal{E}_{I_{1\ldots5}} \leq 150$, is considered to represent a local stiffening within the VF as reported for some structural VF abnormalities or disorders (Hansen and Thibeault, 2006;

* Corresponding author.
E-mail address: annemie.vanhirtum@univ-grenoble-alpes.fr (A. Van Hirtum).

https://doi.org/10.1016/j.jmbbm.2023.105690
Received 20 November 2022; Received in revised form 11 January 2023; Accepted 23 January 2023
Available online 25 January 2023

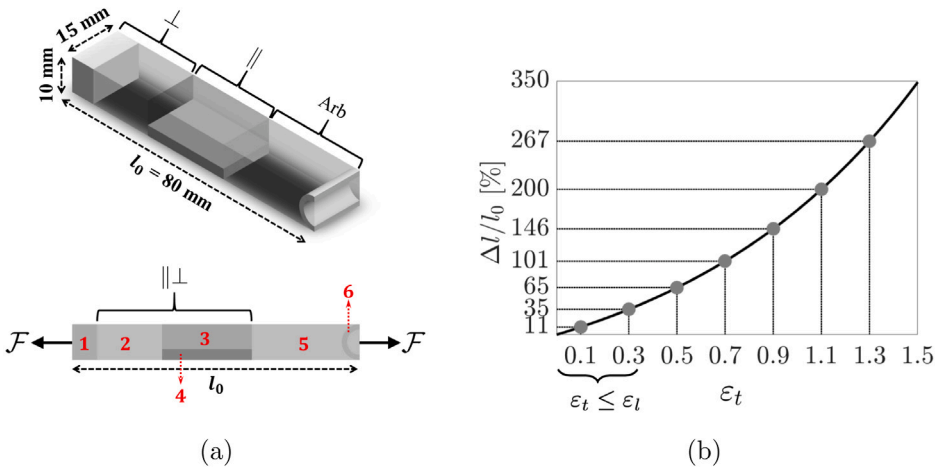

Fig. 1. (a) Illustration of specimen's test section dimensions and different layer stacking with respect to the applied force ($\mathcal{F}$) direction: serial stacking ($\perp$) between layers 1 and 2, parallel ($\parallel$) between 3 and 4, combined ($\parallel\perp$) between 3, 4, and 2 and arbitrary (Arb) between 5 and 6, (b) Degree of deformation $\Delta l/l_0$ for true strain $0 \leq \varepsilon_t \leq 1.5$. The overall low-strain range $\varepsilon_t \leq \varepsilon_l$ with $\varepsilon_l \approx 0.3$ is indicated.

Table 1
Molded single layer properties at room temperature: mixture TE or TD (Mix), mass mixing ratio $\mathcal{M}$, low-strain Young's modulus $\mathcal{E}$ in the strain range $\varepsilon_t \leq \varepsilon_l$.

Label	Composition		$\mathcal{E}$ [kPa]	ε_l
	Mix	$\mathcal{M}$ [–]		
I_1	TE	8:2	2	0.24
I_2	TE	4:2	4	0.41
I_3	TE	2:2	14	0.21
I_4	TE	1:2	23	0.25
I_5	TD	1:2	65	0.16
I_6	TD	0:2	298	0.26

Friedrich et al., 2013; Mattei et al., 2017). Low-strain Young's moduli $\mathcal{E}$ in Table 1 characterising the linear stress–strain curves $\sigma_t(\varepsilon_t)$ at room temperature (21 ± 2 ° C, mean and standard deviation) are obtained as the slope of a linear fit (coefficient of determination $R^2 \geq 98\%$) to the low-strain range with upper low-strain limit ε_l of measured stress–strain curves $\sigma_t(\varepsilon_t)$ gathered from uni-axial tensile tests on molded specimens (Ahmad et al., 2021, 2022).

Despite the anatomical structural relevance of the low-strain elastic Young's moduli $\mathcal{E}$ of the molded silicone layers, so far ML silicone VF replicas (*e.g.* M5, MRI, EPI) are omitted in systematic physical studies on the influence of the VF structure on the FSI due the lack of an *a priori* mechanical characterisation. Recently, in Ahmad et al. (2021, 2022), the low-strain Young's modulus of ML silicone composites for which perfectly bounded adjacent layers are stacked either parallel ($\parallel$), serial ($\perp$), a combination of both ($\parallel\perp$) or arbitrary (Arb) with respect to the force direction as illustrated in Fig. 1(a), is modelled considering the low-strain effective Young's modulus $\mathcal{E}_{eff}$ of an equivalent homogenised composite. This has been obtained by exploiting firstly Voigt's hypothesis (Voigt, 1889) of homogeneous strain for parallel stacked layers and then Reuss's hypothesis (Reuss, 1929) of homogeneous stress for the remaining serial stacked layers. The model approach was extensively validated against measured $\mathcal{E}_{eff}$ values using uni-axial tensile testing (at room temperature) on molded ML specimens with $5 \leq \mathcal{E}_{eff} \leq 40$ kPa. Validation was first done in Ahmad et al. (2021), using $I_{1...5}$, on six two-layer and seven three-layer silicone molded specimens ($5 \leq \mathcal{E}_{eff} \leq 40$ kPa) with parallel ($\parallel$), serial ($\perp$) or combined ($\parallel\perp$) stacking and then in Ahmad et al. (2022), using fourteen specimens obtained as a three-layer composite (I_1, I_2 and I_5) embedding a stiff inclusion (I_6) with variable size, position and stacking. That resulted in more complex specimens with at least four layers which are stacked either parallel ($\parallel$), serial ($\perp$), combined ($\parallel\perp$) or arbitrary (Arb). For each molded specimen in Ahmad et al. (2021, 2022), the low-strain effective Young's modulus $\mathcal{E}_{eff}$ of the equivalent homogenised composite was estimated ($R^2 \geq 96\%$) on the measured stress–strain curves $\sigma_t(\varepsilon_t)$ as the slope characterising the linear low-strain region $\varepsilon_t \leq \varepsilon_l$ with $\varepsilon_l = 0.30 \pm 0.10$. It follows that the low-strain effective Young's modulus $\mathcal{E}_{eff}$, in the strain range up to $\varepsilon_l \approx 0.3$, of an equivalent homogenised ML silicone composite can be accurately modelled (maximum difference of 5.2 kPa (Ahmad et al., 2021, 2022)) from its layers $\mathcal{E}$ and stacking geometry.

The degree of deformation of a specimen of length l_0 and elongation Δl along the force direction,

$$\frac{\Delta l}{l_0} = e^{\varepsilon_t} - 1 \tag{1}$$

associated with the low-strain range up to $\varepsilon_l \approx 0.3$ is limited to deformations up to about 35% as illustrated in Fig. 1(b). As it is well established (Fung, 1967, 2010) that biological soft tissues, and thus human VF tissues (Alipour and Titze, 1991; Min et al., 1995; Zhang et al., 2006; Alipour and Vigmostad, 2012; Miri, 2014), are characterised by small stresses in response to relatively large strains ε_t, greater than one and thus deformations larger than 100% as shown in Fig. 1(b), it is needed to assess how the stress–strain relationship of silicone ML composites behaves beyond the linear range and how the non-linear behaviour compares to the one typically observed in biological soft tissues.

Therefore, in this work, the stress–strain relationship of silicone ML composite specimens is investigated beyond the low-strain elastic range. In particular, 63 measured stress–strain curves on 40 molded specimens from uni-axial stretching at room temperature described in Ahmad et al. (2021, 2022) are further analysed in order to characterise and model the stress–strain curves for $\varepsilon_t > \varepsilon_l$. It is aimed to propose a validated phenomenologically-based continuous *a priori* analytical model of the elastic stress–strain curves within and beyond the elastic low-strain range resulting in analytical models for which model parameters are expressed as a function of the low-strain Young's modulus. Thus, this approach aims to predict the stress–strain behaviour without data fitting to estimate the model parameters. Therefore, the approach is based on continuous hyper-elastic stress–strain models characterised firstly by few (*i.e.* two) model parameters and secondly by a reported accuracy to fit soft biological tissues stress–strain behaviour (Fung, 1967; Demiray, 1972; Tanaka et al., 2011; Fung, 2010; Alipour and Titze, 1991; Burks et al., 2020). It was verified that the best fit accuracy found for the used two-parameter models is similar as the accuracy associated with other hyperelastic models. The total strain range of interest is limited to $\varepsilon_t \leq 1.5$ due to the

Table 2
Molded ML specimens: stacking (||, ⊥, || ⊥, Arb), number of layers n, total number (No.) of specimens and tensile test method (MP or PL), measured low-strain effective Young's modulus $\mathcal{E}_{eff}$ in the range up to $\varepsilon_l \approx 0.3$ at room temperature 21 ± 2 °C.

Stacking	n	No. of ML specimens			$\mathcal{E}_{eff}$ [kPa]
		Total	MP	PL	
||	2	3	3	3	7–33
	3	1	1	1	20
⊥	2	5	3	5	5–29
	3	8	1	8	5 – 38
	4	2	0	2	6
||⊥	3	2	1	2	9–17
	4	4	0	4	27–32
	5	6	0	6	12–31
	7	1	0	1	18
Arb	/	2	0	2	11–20
Overview	≥ 2	34	9	34	6–38

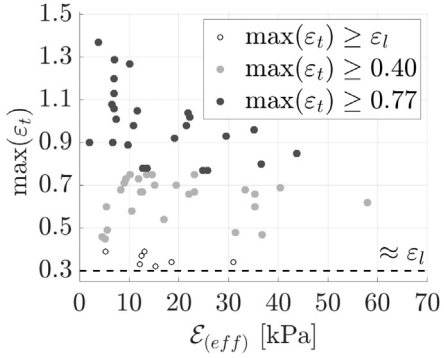

Fig. 2. Measured maximum strain $\max(\varepsilon_t)$ as a function of low-strain Young's modulus $\mathcal{E}_{(eff)}$. The linear low-strain upper limit $\varepsilon_l \approx 0.3$ is indicated (dashed line).

proposed model approach as well as due to the data strain-range used for validation. This corresponds to a degree of deformation $\Delta l/l_0$ up to 350% (see Fig. 1(b)), or about 10 times the maximum elongation of 35% associated with the overall low-strain upper limit $\varepsilon_l = 0.3$.

Experimental methods and measured stress–strain data are briefly outlined in Section 2. In Section 3, continuous two-parameter stress–strain relationships are introduced and analytical parameter expressions are derived. Fitted and analytical stress–strain characterisation on measured data are compared in Section 4. The conclusion is formulated in Section 5.

2. Experimental stress–strain data at room temperature

ML silicone composites are molded using 3D-printed bone-shaped specimen molds (Stratasys ABS-P430, accuracy 0.33 mm). Molded silicone composites have a rectangular test section of length 80 mm, width 15 mm, and height 10 mm as indicated in Fig. 1(a). In total, 40 silicone specimens were molded following the procedure detailed in Ahmad et al. (2021), Bouvet (2019). Six single-layer specimens are molded with one of the silicone mixtures shown in Table 1, which indicates measured low-strain Young's moduli $\mathcal{E}$ and low-strain upper limits ε_l. These 6 silicone mixtures are combined in order to mold 34 ML specimens. Molded layer dimensions are measured using a laser transceiver (Panasonic HL-G112-A-C5, wavelength 655 nm, accuracy 8 μm). Table 2 gives an overview of these ML specimens in terms of their stacking, number of layers n, the uni-axial tension test method (mechanical press MP or/and precision loading PL), and the measured low-strain effective Young's modulus $\mathcal{E}_{eff}$ characterising the low-strain range up to $\varepsilon_l \approx 0.3$. Measured force–elongation data $\mathcal{F}(\Delta l)$ were collected from uni-axial tensile testing at room temperature 21 ± 2 °C. Two methods (MP and PL), previously cross-validated (difference less than 3.5 kPa (Ahmad et al., 2021, 2022)), were used. Briefly, an electro-mechanical press (MP, 3369 Instron Corp.) or a developed precision loading setup (PL) were used to exert the forcing. The mechanical press (MP) was set for displacement control (INSTRON 3369 series, precision of ±0.2 mm at least) up to maximum elongations of 100 mm and 150 mm following the procedure detailed in Ahmad et al. (2021). The deformation rate was set to 1 mm/s and 2 mm/s for the 100 mm and 150 mm elongation respectively. Force and elongation time series (sampling rate of 10 Hz) were measured during loading and unloading of the specimens. No plastic deformation was observed following unloading. Additional cross-sectional area measurements are made for each specimen without loading and for elongations set to 25, 50, 100 and 150 mm. For the developed PL setup (Ahmad et al., 2021), the force is the controlled parameter and is exerted by adding precision loads (PL) of mass m (Vastar 500G X 0.01G, accuracy 0.01 g) at a single rate for each specimen, while measuring the elongation at every force increment with an accuracy of 0.05 mm as described in Ahmad et al. (2021, 2022). Depending on the specimen, total added weight ranges from 46 to 426 g, corresponding to a total elongation from 23 up to 255 mm. The cross-sectional area is measured whenever the elongation increment due to added weights yields about 15 ± 5 mm. For both methods, the cross-sectional area $\mathcal{A}$ is measured with an accuracy of 0.02 mm. A quadratic fit (coefficient of determination $R^2 \geq 99\%$) is used to have a continuous approximation of the average area-elongation relationship $\mathcal{A}^q(\Delta l)$ for each specimen. The incompressibility of the specimens was verified by estimating the area-elongation relationship as $\mathcal{A} = \mathcal{A}_0 l_0/l$ ($R^2 \geq 84\%$), with $\mathcal{A}_0$ denoting the initial cross-sectional area of the specimen and $l = l_0 + \Delta l$ the length of the specimen. The longitudinal stress σ_t and strain ε_t are then obtained as

$$\sigma_t = \frac{\mathcal{F}}{\mathcal{A}^q}, \tag{2}$$

$$\varepsilon_t = \ln\left(\frac{l_0 + \Delta l}{l_0}\right), \tag{3}$$

using measured elongation Δl, force $\mathcal{F}$, and area $\mathcal{A}^q$ and with length l_0 and deformation Δl as defined in Eq. (1). Here, the true definitions of stress and strain, which are based on the instantaneous values of length and cross-section area, are adopted. The measured maximum strain $\max(\varepsilon_t)$ depends on the specimen and is limited to $\max(\varepsilon_t) \leq 1.36$. An overview of $\max(\varepsilon_t)$ as a function of $\mathcal{E}_{(eff)}$ is given in Fig. 2. Respectively, 52 and 25 of the measured stress–strain data curves satisfy $\max(\varepsilon_t) \geq 0.4$ and $\max(\varepsilon_t) \geq 0.77$, which corresponds to an extension of the strain range of about 33% and 156% beyond the upper limit of the low-strain region $\varepsilon_l \approx 0.3$.

3. Continuous elastic stress–strain relationships and *a priori* modelled parameter expressions

3.1. Continuous two-parameter relationships

The typical stress–strain data curve plotted in Fig. 3(a) shows that the elastic linear low-strain range $\varepsilon_t \leq \varepsilon_l$, expressed with Hooke's law using the low-strain effective Young's modulus $\mathcal{E}_{(eff)}$ as

$$\sigma_t(\varepsilon_t) = \mathcal{E}_{(eff)}\,\varepsilon_t, \tag{4}$$

transitions to a more rapid increase of stress σ_t with strain ε_t indicating elastic non-linear stress–strain behaviour for $\varepsilon > \varepsilon_l$. In accordance with models proposed for soft biological tissues accounting for the rapid non-linear increase of stress with strain for $\varepsilon_t > \varepsilon_l$ (Fung, 1967; Demiray, 1972; Tanaka et al., 2011; Fung, 2010; Alipour and Titze, 1991; Burks et al., 2020), the exponential and third order polynomial (cubic) non-linear continuous two-parameter relationships with C^1 continuity are

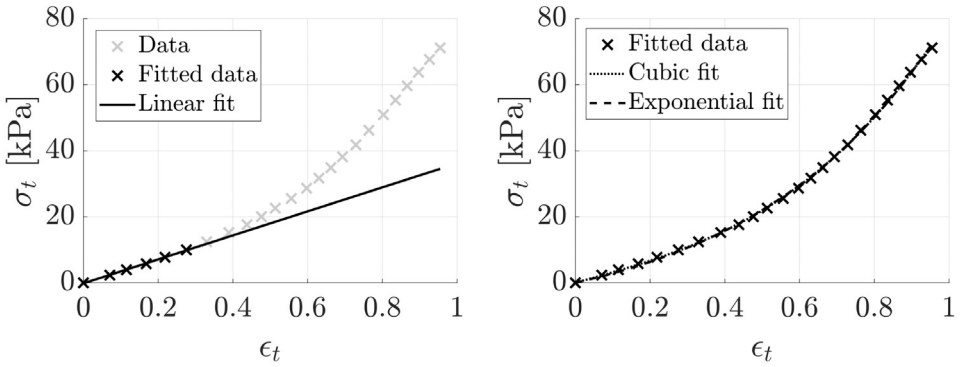

(a) Linear model (b) Non-linear models

Fig. 3. Experimental stress–strain data curve $\sigma_t(\varepsilon_t)$ (symbols) and stress–strain models (lines) with fit accuracy $R^2 \geq 99.5\%$ for a five-layer ($n = 5$) specimen with combined ($\|\perp$) stacking: (a) linear (full line) low-strain ($\varepsilon_t \leq \varepsilon_l$) fit with slope $\mathcal{E}_{eff} = 36$ kPa, (b) continuous non-linear cubic (dotted line) and exponential (dashed line) fits.

assessed in order to represent stress–strain curves $\sigma_t(\varepsilon_t)$ of the ML composites:

$$\text{exponential}: \sigma_t(\varepsilon_t) = A\,(e^{B\,\varepsilon_t} - 1), \tag{5a}$$

$$\text{cubic}: \sigma_t(\varepsilon_t) = a\,\varepsilon_t^3 + b\,\varepsilon_t, \tag{5b}$$

with (A, B) and (a, b) their respective two parameter sets.

Fig. 3 illustrates the linear fit of Eq. (4) (in Fig. 3(a)) to the low-strain region $\varepsilon_t \leq \varepsilon_l$ and the continuous exponential and cubic fits of Eq. (5) (in Fig. 3(b)) to a typical measured stress–strain data set. For each measured stress–strain curve, best fit parameter sets $(\widehat{A}, \widehat{B})$ and $(\widehat{a}, \widehat{b})$ are estimated by minimising the root mean square error (rmse),

$$\text{rmse} = \sqrt{\frac{1}{N}\sum_{i=1}^{N}\left[(\widehat{\sigma}_t)_i - (\sigma_t)_i\right]^2} \tag{6}$$

between measured σ_t and fitted $\widehat{\sigma}_t$ stresses with N the number of strain data points within the analysis range and i the index of individual data points. The goodness of fit, expressed by the coefficient of determination R^2, yields $R^2 > 99.5\%$ for each continuous model to the measured stress–strain curves, obtained using either MP or PL uni-axial tensile testing. Therefore, both continuous two-parameter relationships can be used to provide an accurate estimation of the measured stress–strain curves. The linear low-strain (Section 3.2) and non-linear (Section 3.3) behaviour of these relationships in terms of their parameters is considered next.

3.2. Modelled low-strain behaviour of continuous stress–strain relationships

The first order derivatives of Eqs. (5a) and (5b) with respect to ε_t become

$$\text{exponential}: \frac{d\sigma_t}{d\varepsilon_t} = A\,B\,e^{B\,\varepsilon_t}, \tag{7a}$$

$$\text{cubic}: \frac{d\sigma_t}{d\varepsilon_t} = 3\,a\,\varepsilon_t^2 + b. \tag{7b}$$

The linear low-strain behaviour for $\varepsilon_t \leq \varepsilon_l$ of the exponential Eq. (5a) and cubic Eq. (5b) relationship is then obtained from the first order Taylor expansion near $\varepsilon_t \approx 0$ as:

$$\text{exponential}: \sigma_t(\varepsilon_t \approx 0) = A\,B\,\varepsilon_t, \tag{8a}$$

$$\text{cubic}: \sigma_t(\varepsilon_t \approx 0) = b\,\varepsilon_t, \tag{8b}$$

where it is used that both the exponential and cubic relationships have no residual stress at zero strain so that $\sigma_t(\varepsilon_t \approx 0) \approx 0$ kPa. Consequently, the elastic low-strain (effective) Young's modulus $\mathcal{E}_{(eff)}$, describing the linear stress–strain behaviour in the low-strain range $\varepsilon_t \leq \varepsilon_l$ (Eq. (4)) can be expressed in terms of the parameters of the continuous relationships as:

$$\text{exponential}: \mathcal{E}_{(eff)} = A\,B, \tag{9a}$$

$$\text{cubic}: \mathcal{E}_{(eff)} = b. \tag{9b}$$

3.3. Modelled non-linear behaviour of continuous stress–strain relationships

Using $A = \mathcal{E}_{(eff)}/B$ (Eq. (9a)) and $b = \mathcal{E}_{(eff)}$ (Eq. (9b)) and assuming that low-strain linear Young's modulus $\mathcal{E}_{(eff)}$ is a known quantity, the two-parameter relationships of Eq. (5a) and (5b) can be rewritten as one-parameter relationships

$$\text{exponential}: \sigma_t(\varepsilon_t) = \frac{\mathcal{E}_{(eff)}}{B}\,(e^{B\,\varepsilon_t} - 1), \tag{10a}$$

$$\text{cubic}: \sigma_t(\varepsilon_t) = a\,\varepsilon_t^3 + \mathcal{E}_{(eff)}\,\varepsilon_t, \tag{10b}$$

with the unknown parameters B and a (already in Eq. (5)) determining the non-linear behaviour in the range $\varepsilon_t > \varepsilon_l$.

From the first order expansion of the relationships in Eq. (5) follows that the local linear slopes $\mathcal{E}_{NL}$ associated with their linear approximations near any ε_t are expressed as:

$$\text{exponential}: \mathcal{E}_{NL} = \mathcal{E}_{(eff)}\,e^{B\,\varepsilon_t}, \tag{11a}$$

$$\text{cubic}: \mathcal{E}_{NL} = 3\,a\,\varepsilon_t^2 + \mathcal{E}_{(eff)}. \tag{11b}$$

At low-strain (for $\varepsilon_t \approx 0$), these expressions reduce to $\mathcal{E}_{NL}(\varepsilon_t \approx 0) \approx \mathcal{E}_{(eff)}$ in accordance with the linear low-strain behaviour described in Section 3.2.

In Section 3.1 is shown that both the exponential (Eq. (10a)) and cubic (Eq. (10b)) relationship can provide accurate estimations of the measured stress–strain data sets as the fit accuracy holds $R^2 > 99.5\%$. Therefore, estimated stresses obtained with both relationships are assumed to match. Equating Eq. (10a) and (10b) for any matching strain value ε_t^m and making use of Eqs. (11a) and (11b) gives the following relationship between $\mathcal{E}_{NL}$ and the low-strain Young's modulus $\mathcal{E}_{(eff)}$

$$\mathcal{E}_{NL}\,\ln\left(\frac{\mathcal{E}_{NL}}{\mathcal{E}_{(eff)}}\right) + 2\,\mathcal{E}_{(eff)}\,\ln\left(\frac{\mathcal{E}_{NL}}{\mathcal{E}_{(eff)}}\right) - 3\,\mathcal{E}_{NL} + 3\,\mathcal{E}_{(eff)} = 0. \tag{12}$$

In Fig. 4 is shown that the solution $\mathcal{E}_{NL}(\mathcal{E}_{(eff)})$ is accurately approximated as $\mathcal{E}_{NL} = 8.58\,\mathcal{E}_{(eff)}$ ($R^2 = 99.9\%$) for $\mathcal{E}_{(eff)} \in [0.1, 350]$, which includes the range of interest indicated in Table 1 and in Table 2.

The two-parameter sets (A, B) and (a, b) of the non-linear exponential and cubic relationships at any matching strain value ε_t^m are then *a*

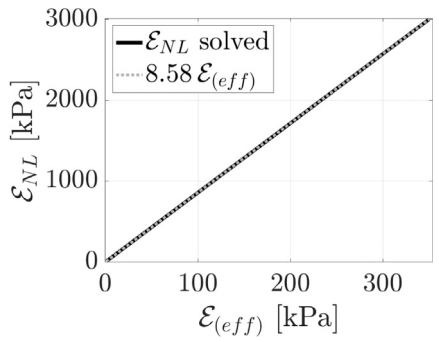

Fig. 4. Solutions $\mathcal{E}_{NL}$ from Eq. (12) as a function of $\mathcal{E}_{(eff)}$ (thick full line) and linear fit (light dotted line) with $R^2 = 99.9\%$. Both curves superimpose.

priori given in terms of $\mathcal{E}_{(eff)}$ and $\mathcal{E}_{NL}$ as,

$$\text{exponential}: \quad B = \frac{1}{\varepsilon_t^m} \ln\left(\frac{\mathcal{E}_{NL}}{\mathcal{E}_{(eff)}}\right), \qquad A = \frac{\varepsilon_t^m \, \mathcal{E}_{(eff)}}{\ln\left(\frac{\mathcal{E}_{NL}}{\mathcal{E}_{(eff)}}\right)}, \tag{13a}$$

$$\text{cubic}: \quad b = \mathcal{E}_{(eff)}, \qquad a = \frac{\mathcal{E}_{NL} - \mathcal{E}_{(eff)}}{3\,(\varepsilon_t^m)^2}. \tag{13b}$$

Using the ratio $\mathcal{E}_{NL}/\mathcal{E}_{(eff)} \approx 8.58$, the two-parameter sets of Eq. (5) become:

$$\text{exponential}: \quad B \approx 2.15\,\frac{1}{\varepsilon_t^m}, \qquad A \approx 0.47\,\mathcal{E}_{(eff)}\,\varepsilon_t^m, \tag{14a}$$

$$\text{cubic}: \quad b \approx \mathcal{E}_{(eff)}, \qquad a \approx 2.53\,\mathcal{E}_{(eff)}\,\frac{1}{(\varepsilon_t^m)^2}. \tag{14b}$$

These *a priori* modelled (positive) parameter expressions respect the low-strain behaviour in Eqs. (9a) and (9b) as $A\,B \approx \mathcal{E}_{(eff)}$ and $b \approx \mathcal{E}_{(eff)}$. Beyond the low-strain region, the cubic parameter a and the exponential parameter A are proportional to $\mathcal{E}_{(eff)}$. In addition, the cubic parameter a and exponential parameters (A, B) not only depend on $\mathcal{E}_{(eff)}$, but also on the considered strain ε_t^m at which the cubic and exponential model are imposed to match. Note that from a third order Taylor series expansion of the exponential function given in Eq. (10a) follows that, under the condition that the quadratic term of the expansion is negligible compared to the linear or cubic expansion term, nearly matching of the exponential and cubic functions in Eq. (5) leads to the condition $a = \frac{1}{6}B^2\mathcal{E}_{(eff)}$, which is the case considering expressions a and B in Eq. (14).

For $\varepsilon_t^m = 1$, this gives $B \approx 2.15$, $A/\mathcal{E}_{(eff)} \approx 0.5$ and $a/\mathcal{E}_{(eff)} \approx 2.5$. For $\varepsilon_t^m \neq 1$, the model parameters B, A and a will decrease or increase with respect to their value at $\varepsilon_t^m = 1$, depending on $\varepsilon_t^m < 1$ or $\varepsilon_t^m > 1$, since $B \propto \varepsilon_t^{-1}$, $A \propto \varepsilon_t$ and $a \propto \varepsilon_t^{-2}$. Consequently, the influence of the value of matching strain ε_t^m needs to be considered.

The relative difference (in percentage) between the estimated true stresses using the exponential (σ_t^e) and cubic (σ_t^c) relationships with the modelled parameter values (Eq. (14)) as a function of the normalised strain $\varepsilon_t/\varepsilon_t^m$ for any ε_t^m is plotted in Fig. 5(a). The difference is zero at $\varepsilon_t/\varepsilon_t^m \in \{0, 1\}$ as for these strains the stresses match. For $0 \leq \varepsilon_t/\varepsilon_t^m \leq 1$, the difference is less than the maximum of 12.6% associated with $\varepsilon_t/\varepsilon_t^m = 0.28$. For $\varepsilon_t/\varepsilon_t^m > 1$, the difference increases since σ_t^e (exponential) increases more rapidly than σ_t^c (cubic). Overall, the stress-difference remains less than 12.6% when fulfilling the condition $\varepsilon_t/\varepsilon_t^m \leq 1.55$ and increases thereafter. Thus ε_t^m should be at least 65% of the maximum assessed strain $\max(\varepsilon_t)$ to ensure this accuracy between both the exponential and cubic curves obtained with modelled parameters from Eq. (14). For $0.77 \leq \varepsilon_t^m \leq 1.36$, which is reasonable considering the variation of the maximum strain ($\max(\varepsilon_t) \leq 1.36$) in the measured stress–strain curves (see Fig. 2), we get using Eq. (14) the model parameter ranges $1.58 \leq B \leq 2.79$, $0.36 \leq A/\mathcal{E}_{(eff)} \leq 0.64$, $1.36 \leq a/\mathcal{E}_{(eff)} \leq 4.27$ and $b = \mathcal{E}_{(eff)}$. For convenience, concretely $\varepsilon_t^m = 1$ is considered so that Eq. (14) provides *a priori* modelled expressions of the two-parameter sets as a function of $\mathcal{E}_{(eff)}$ only.

Introducing the elongation parameter $\lambda = l/l_0$ so that $\lambda = e^{\varepsilon_t}$ and $\lambda \geq 1$, the strain energy density function expressing the strain energy per unit volume of the deformed material is obtained as the work done by the load

$$\mathcal{W}(\lambda) = \int_1^{\lambda} \frac{\sigma_t(\lambda)}{\lambda^2} d\lambda. \tag{15}$$

Inserting the exponential σ_t^e and the cubic σ_t^c stress relationship with the modelled parameters expressions of Eq. (14), $\mathcal{W}$ normalised by the linear low-strain modulus $\mathcal{E}_{(eff)}$ becomes,

$$\text{exponential}: \quad \frac{\mathcal{W}^e(\lambda)}{\mathcal{E}_{eff}} \approx 0.47\left(\frac{\lambda^{1.15}}{1.15} + \frac{1}{\lambda} - 1.87\right), \tag{16a}$$

$$\text{cubic}: \quad \frac{\mathcal{W}^c(\lambda)}{\mathcal{E}_{eff}} \approx -\frac{1}{\lambda}\left(2.53\,\ln^3(\lambda) + 7.59\,\ln^2(\lambda) + 16.18\,\ln(\lambda) + 16.18\right). \tag{16b}$$

$\mathcal{W}^e$ and $\mathcal{W}^c$ are plotted in Fig. 5(b) as a function of $\varepsilon_t/\varepsilon_t^m$. As observed, the curves are similar within the range $0 \leq \varepsilon_t/\varepsilon_t^m \leq 1.55$ because the normalised difference $(\mathcal{W}^e - \mathcal{W}^c)/\mathcal{W}^e$ is limited to within 12.6% with a single maximum at $\varepsilon_t/\varepsilon_t^m = 0.39$.

4. Stress–strain characterisation

4.1. Parameter values: best fit, best fit approximation and a priori modelled

Best fit parameter values obtained by minimising the rmse (Eq. (6)) between the continuous exponential ($\hat{a}$ and $\hat{b}$) or cubic ($\hat{A}$ and $\hat{B}$) fits for $\hat{\sigma}_t(\varepsilon_t)$ and the measured stress–strain curves $\sigma_t(\varepsilon_t)$ for the complete strain range up to $\max(\varepsilon_t)$ are plotted in Fig. 6 as a function of the low-strain Young's modulus $\mathcal{E}_{(eff)}$. As detailed in Section 3.3, the best fit accuracy yields $R^2 > 99.5\%$ for all specimens so that both the exponential and cubic two-parameter relationships provide accurate estimates of the measured stress–strain data curves.

As the rmse-minimisation is a constraint optimisation, resulting best fit parameter estimations depend on the extent of the strain range $\varepsilon_t \leq \max(\varepsilon_t)$ and thus on $\max(\varepsilon_t)$. This is shown in Fig. 6 for best fit parameter estimations on data sets with $\max(\varepsilon_t) \geq 0.40$ (light grey dots) and $\max(\varepsilon_t) \geq 0.77$ (dark grey dots). Best fit parameter estimations $\hat{A}$, $\hat{B}$ and $\hat{a}$ for data sets with $\max(\varepsilon_t) \geq 0.77$ can be approximated (dashed black lines) as :

$$\hat{A} \approx 0.33\,\mathcal{E}_{(eff)}, \qquad \text{(fit accuracy } R^2 = 84\%), \tag{17a}$$

$$\hat{B} \approx 2.21, \qquad \text{(mean with standard deviation} \pm 0.52), \tag{17b}$$

$$\hat{a} \approx 1.78\,\mathcal{E}_{(eff)}, \qquad \text{(fit accuracy } R^2 = 83\%). \tag{17c}$$

In accordance with *a priori* modelled parameter expressions, (A, B) in Eq. (14a) and a in Eq. (14b), approximations of best fit parameters $\hat{A}$ and $\hat{a}$ depend linearly on the low-strain Young's modulus $\mathcal{E}_{(eff)}$ whereas $\hat{B}$ is approximately constant. For comparison, modelled parameter ranges for $0.77 \leq \varepsilon_t^m \leq 1.36$ ($1.58 \leq B \leq 2.79$, $0.36 \leq A/\mathcal{E}_{(eff)} \leq 0.64$, $1.36 \leq a/\mathcal{E}_{(eff)} \leq 4.27$) are indicated (shaded regions). Thus, best fit parameters and their approximations are of the order of magnitude of the modelled parameters.

Following the modelled expressions in Eq. (9), the linear low-strain stress behaviour is determined by the cubic parameter b (Eq. (9a)) or the exponential parameter product AB (Eq. (9b)). Therefore, the best fit parameter $\hat{b}$ (light grey dots), the product $\hat{A}\hat{B}$ (dark grey dots) as well as the low-strain Young's modulus $\mathcal{E}_{(eff)}$ (full line, identity function) are plotted as a function of $\mathcal{E}_{(eff)}$ for all data sets in Fig. 6(d). It is seen

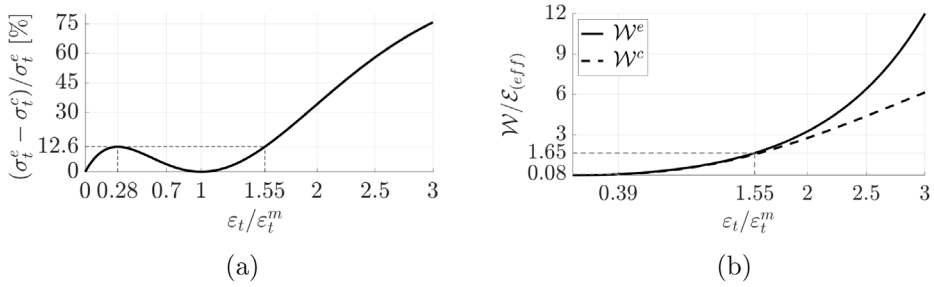

Fig. 5. For the exponential (superscript e) and cubic (superscript c) relationship: (a) relative difference (%) between modelled true stresses σ_t as a function of normalised strain $\varepsilon_t/\varepsilon_t^m$, (b) strain energy density function $\mathcal{W}$ normalised by low-strain $Y_{(eff)}$.

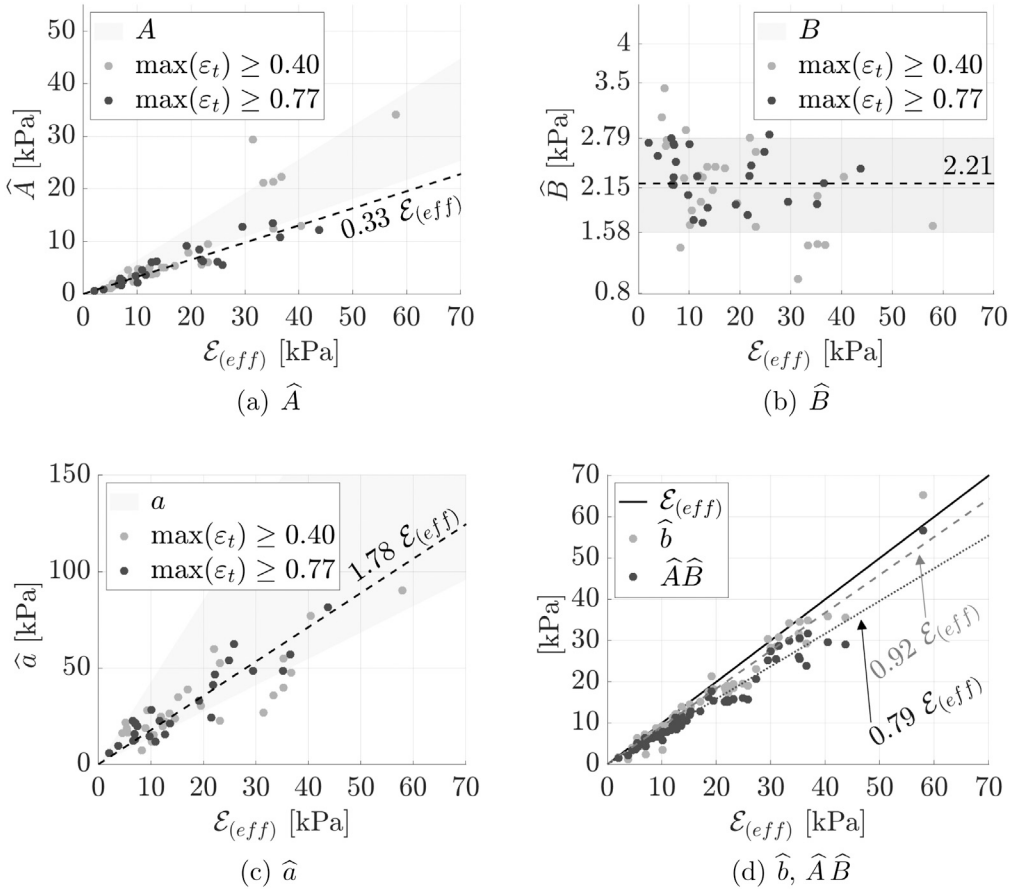

Fig. 6. Exponential $(\widehat{A}, \widehat{B})$ and cubic $(\widehat{a}, \widehat{b})$ best fit ($R^2 > 99.5\%$) parameters to measured stress–strain curves in the range $\varepsilon_t \leq \max(\varepsilon_t)$ as a function of $\mathcal{E}_{(eff)}$: (a) $\widehat{A}$ for $\max(\varepsilon_t) \geq \{0.40, 0.77\}$, (b) $\widehat{B}$ for $\max(\varepsilon_t) \geq \{0.40, 0.77\}$, (c) $\widehat{a}$ for $\max(\varepsilon_t) \geq \{0.40, 0.77\}$ and (d) $\widehat{b}$, $\widehat{A}\,\widehat{B}$ and $\mathcal{E}_{(eff)}$. In (a,b,c) shaded regions indicate modelled parameter ranges for $0.77 \leq \varepsilon_t^m \leq 1.36$, dashed lines show fitted parameter approximations for $\max(\varepsilon_t) \geq 0.77$. In (d) the identity function (full line) and linear fits (dashed and dotted line) are plotted.

that $\widehat{b}$ and $\widehat{A}\widehat{B}$ can be approximated as

$$\widehat{b} \approx 0.92\ \mathcal{E}_{(eff)}, \qquad \text{(fit accuracy } R^2 = 95\%\text{)}, \tag{18a}$$

$$\widehat{A}\,\widehat{B} \approx 0.79\ \mathcal{E}_{(eff)}, \qquad \text{(fit accuracy } R^2 = 94\%\text{)}. \tag{18b}$$

As the slopes 0.92 and 0.79 are smaller than one, $\widehat{b}$ and $\widehat{A}\widehat{B}$ underestimate the measured low-strain Young's modulus $\mathcal{E}_{(eff)}$ with 8% and 21% respectively. Note that for the exponential best fit parameters $\widehat{A}$ and $\widehat{B}$ a trade-off can be observed from Figs. 6(a) and 6(b) since *e.g.* for $\mathcal{E}_{(eff)} \approx 32$ kPa large values of $\widehat{A}$ are compensated by low values of $\widehat{B}$ and vice-versa. This trade-off partly explains the slightly reduced performance of the exponential best fit compared to the cubic one within the low-strain region in order to predict $\mathcal{E}_{(eff)}$. The mean and standard deviation between the measured $\mathcal{E}_{(eff)}$ and best fit parameter estimations ($\widehat{b}$ and $\widehat{A}\,\widehat{B}$) mounts to 3.7 ± 2.8 kPa (exponential) and 1.9 ± 1.8 kPa (cubic). The accuracies of the measurement (3.5 kPa, see Section 2) or the model (5.2 kPa, see Section 1) of the low-strain Young's modulus $\mathcal{E}_{(eff)}$ are of the same order of magnitude so that, in particular, the cubic best fit parameter $\widehat{b}$ provides an accurate estimation of $\mathcal{E}_{(eff)}$.

Thus, the parameter values of the cubic and exponential relationships can be estimated in three different ways. Besides the best fit parameters sets (exponential $(\widehat{A}, \widehat{B})$ or cubic $(\widehat{a}, \widehat{b})$), best fit parameter approximations as a function of $\mathcal{E}_{(eff)}$ are obtained combining Eqs. (17) and (18a) whereas *a priori* modelled parameter values are obtained as a function of $\mathcal{E}_{(eff)}$ from Eq. (14) with for convenience $\varepsilon_t^m = 1$ as outlined in Section 3.3 (Fig. 5).

As the best fit parameter approximations and the *a priori* modelled parameters both depend solely on the low-strain Young's modulus $\mathcal{E}_{(eff)}$, the fit accuracy might vary when either measured $\mathcal{E}_{eff}$ or modelled $\widehat{\mathcal{E}}_{eff}$ (as outlined in Ahmad et al. (2021, 2022)) effective Young's

Table 3
Mean and standard deviation of the accuracy (R^2 in %) of cubic and exponential two-parameter relationships to stress–strain data using either best fit parameters (dark dots in Fig. 6), best fit approximated parameters (Eqs. (17) and (18a)), or *a priori* modelled parameters at $\varepsilon_t^m = 1$ (Eq. (14)) for data sets with $\max(\varepsilon_t) \geq \{\varepsilon_l, 0.40, 0.77\}$.

	Best fit		Approximations		Modelled with $\varepsilon_t^m = 1$	
	Cubic	Exponential	Cubic	Exponential	Cubic	Exponential
$\max(\varepsilon_t) \geq \varepsilon_l$	99.9 ± 0.1	99.9 ± 0.1	98 ± 2^a 95 ± 5^b	98 ± 2^a 94 ± 5^b	92 ± 10^a 91 ± 13^b	87 ± 12^a 87 ± 19^b
$\max(\varepsilon_t) \geq 0.40$	99.8 ± 0.2	99.8 ± 0.1	98 ± 2^a 95 ± 5^b	98 ± 2^a 94 ± 5^b	90 ± 11^a 91 ± 16^b	86 ± 13^a 89 ± 16^b
$\max(\varepsilon_t) \geq 0.77$	99.8 ± 0.2	99.8 ± 0.1	97 ± 3^a 95 ± 4^b	98 ± 3^a 95 ± 4^b	88 ± 12^a 89 ± 16^b	85 ± 14^a 87 ± 18^b

[a]Using measured low-strain $\mathcal{E}_{eff}$.
[b]Using modelled low-strain $\hat{\mathcal{E}}_{eff}$ (Ahmad et al., 2021, 2022).

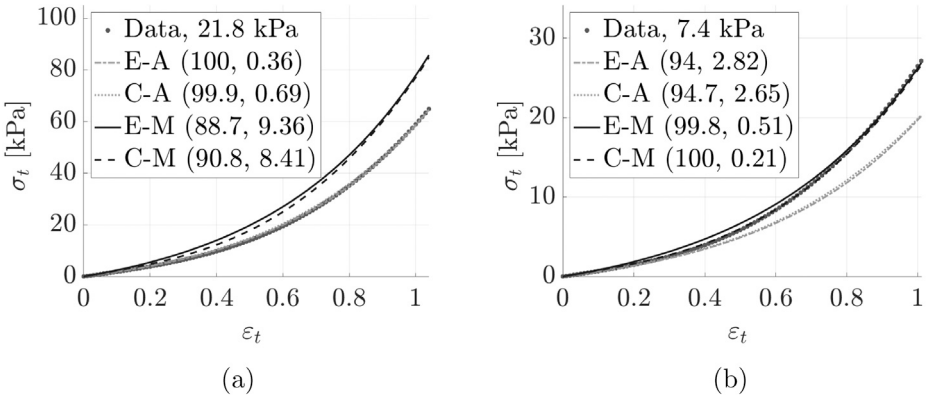

Fig. 7. Examples of measured stress–strain data (symbols) and $\mathcal{E}_{eff}$ (in kPa), resulting cubic (C··) and exponential (E··) fits with the best fit approximation parameter sets (··A) and the modelled parameter sets (··M) for three-layered silicone composites with: (a) serial ($\perp$) stacking and (b) combined ($\parallel\perp$) stacking. The fit accuracy (R^2, rmse) with R^2 (in %) and root mean square error rmse (in kPa) is indicated for each fit. In (a) curves E–A and C–A overlap measured data. In (b) E–A and C–A as well as C–M and measured data overlap.

modulus values for ML silicone composites are used. Examples of cubic (C··) and exponential (E··) fits for three-layered specimens with the best fit parameter approximation sets (··A) and the modelled parameter sets (··M) are plotted in Fig. 7. An overview of the exponential and cubic fit accuracies for the different parameter sets for all stress–strain data curves is given in Table 3 where the mean and standard deviation of R^2 are reported. Overall, both the cubic and exponential fits exhibit similar tendencies. The overall mean fit performance is at least $R^2 \geq 85\%$ illustrating that all parameter sets can be used to obtain a continuous fit of the measured stress–strain curves. For modelled $\hat{\mathcal{E}}_{eff}$, best fit parameter approximations and modelled parameters result in mean R^2 values of respectively more than 94% and 85%. Consequently, these parameter estimations in combination with the model of the low-strain effective Young's modulus outlined in Ahmad et al. (2021, 2022) can be used to obtain an *a priori*, and hence measurement free, characterisation of stress–strain curves up to $\varepsilon_t \leq 1.5$ for ML silicone composites.

4.2. Accounting for a linear high-strain elastic region

Fit accuracies reported in Table 3 for the continuous exponential and cubic relationships, inspired on stress–strain models proposed for soft biological tissues (Fung, 1967; Demiray, 1972; Tanaka et al., 2011; Fung, 2010; Alipour and Titze, 1991; Burks et al., 2020), suggest that ML silicone composites behave, at least partly, in a similar manner. For soft tissues, the continuous stress–strain behaviour is generally described as consisting of an exponential strain range, which includes the linear low-strain elastic range, followed by a linear elastic high-strain range. Eq. (12), for which the solution is plotted in Fig. 4, suggests that the high-strain elastic Young's modulus $\mathcal{E}_{NL}$ can be expressed as a linear function of the low-strain elastic Young's modulus $\mathcal{E}_{(eff)}$ with slope 8.58. Since this relationship $\mathcal{E}_{NL} = 8.58\,\mathcal{E}_{(eff)}$ underlies the modelled parameters for which the mean fit accuracy amounts to $R^2 \geq 85\%$, the high-strain elastic region $\varepsilon_t \geq \varepsilon_t^{NL}$ is explicitly accounted for by considering high-strain onset ε_t^{NL} and high-strain Young's modulus $\mathcal{E}_{NL}$. In the range $\varepsilon_t \leq \varepsilon_t^{NL}$, the stress is as before described using the continuous two-parameter exponential and cubic relationships defined in Eq. (5). Best fit parameter estimations are again obtained by minimising the rmse given in Eq. (6). Overall, it is found that the best fit accuracy is slightly improved, at the cost of two additional parameters, from $R^2 \geq 99.5\%$ to $R^2 \geq 99.6$ % for the cubic and to $R^2 \geq 99.7\%$ for the exponential relationship, respectively. An example of best fits with (EO) and without (E) high-strain linear elastic range is plotted in Fig. 8.

When accounting explicitly for a linear high-strain stress behaviour, expressions in Eqs. (17) and (18) become

$$\hat{A} \approx 0.40\ \mathcal{E}_{(eff)}, \qquad \text{(fit accuracy } R^2 = 87\%), \tag{19a}$$

$$\hat{B} \approx 2.07, \qquad \text{(mean with standard deviation} \pm 0.67), \tag{19b}$$

$$\hat{a} \approx 1.60\ \mathcal{E}_{(eff)}, \qquad \text{(fit accuracy } R^2 = 74\%) \tag{19c}$$

and

$$\hat{b} \approx 0.92\ \mathcal{E}_{(eff)}, \qquad \text{(fit accuracy } R^2 = 98\%), \tag{20a}$$

$$\hat{A}\,\hat{B} \approx 0.81\ \mathcal{E}_{(eff)}, \qquad \text{(fit accuracy } R^2 = 98\%). \tag{20b}$$

Thus, cubic and exponential best fit parameters can again be approximated as a constant or linear function of the low-strain elastic Young's modulus $\mathcal{E}_{(eff)}$. Comparing expressions of $\hat{b}$ and $\hat{A}\,\hat{B}$ in Eq. (18) with those in Eq. (20) shows that the best fit approximations, describing the linear low-strain behaviour ($\varepsilon_t \leq \varepsilon_l$), remain similar since the

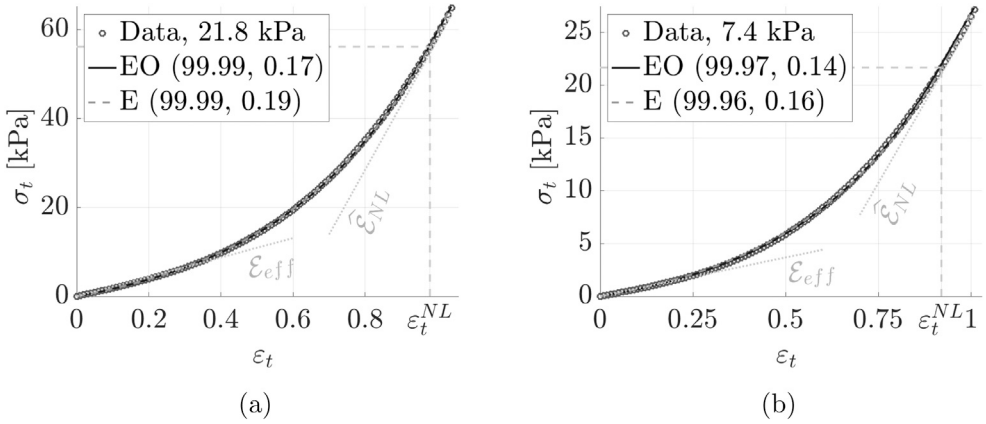

Fig. 8. Examples of measured stress–strain data (symbols) and low-strain linear slope $\mathcal{E}_{eff}$ (in kPa) and resulting exponential best fits without (E) and with (EO) linear high strain range with slope $\hat{\mathcal{E}}_{NL}$ and onset ε_t^{NL} for three-layered silicone composites with: (a) serial ($\perp$) stacking, $\mathcal{E}_{eff} = 21.8$ kPa, $\hat{\mathcal{E}}_{NL} = 145.6$ kPa and $\varepsilon_t^{NL} = 0.98$, (b) combined ($\parallel\perp$) stacking, $\mathcal{E}_{eff} = 7.4$ kPa, $\hat{\mathcal{E}}_{NL} = 60.1$ kPa and $\varepsilon_t^{NL} = 0.92$. The fit accuracy ($R^2$, rmse) with R^2 (in %) and root mean square error rmse (in kPa) is indicated for each fit.

Table 4
Mean and standard deviation of the accuracy (R^2 in %) of non-linear cubic and exponential two-parameter and linear two-parameter high-strain relationships to stress–strain data using either best fit parameters, best fit approximated parameters or *a priori* modelled parameters at $\varepsilon_t^m = \varepsilon_t^{NL}$ and $\varepsilon_t^{NL} = 0.85\ \max(\varepsilon_t)$ for data sets with $\max(\varepsilon_t) \geq \{\varepsilon_l, 0.40, 0.77, 0.90\}$.

	Best fit		Approximations		Modelled with $\varepsilon_t^m = \varepsilon_t^{NL}$	
	Cubic	Exponential	Cubic	Exponential	Cubic	Exponential
$\max(\varepsilon_t) \geq \varepsilon_l$	99.9 ± 0.1	99.9 ± 0.1	98 ± 2[a] 89 ± 13[b]	98 ± 2[a] 87 ± 17[b]	28 ± 37[a] 31 ± 36[b]	27 ± 36[a] 32 ± 36[b]
$\max(\varepsilon_t) \geq 0.40$	99.9 ± 0.1	99.9 ± 0.1	98 ± 2[a] 92 ± 7[b]	98 ± 2[a] 91 ± 10[b]	32 ± 38[a] 39 ± 36[b]	31 ± 37[a] 37 ± 36[b]
$\max(\varepsilon_t) \geq 0.77$	99.9 ± 0.1	99.9 ± 0.1	98 ± 2[a] 94 ± 4[b]	98 ± 2[a] 94 ± 7[b]	52 ± 39[a] 64 ± 31[b]	54 ± 39[a] 62 ± 32[b]
$\max(\varepsilon_t) \geq 0.90$	99.9 ± 0.1	99.9 ± 0.1	98 ± 2[a] 94 ± 5[b]	98 ± 2[a] 94 ± 7[b]	71 ± 33[a] 61 ± 37[b]	69 ± 33[a] 60 ± 37[b]

[a]Using measured $\mathcal{E}_{eff}$, $\mathcal{E}_{NL}$ and ε_t^{NL}.

[b]using modelled $\hat{\mathcal{E}}_{eff}$ (Ahmad et al., 2021, 2022), $\mathcal{E}_{NL}$ and ε_t^{NL}.

slopes vary with less than 2.5%. The change to best fit parameter approximations $\hat{a}$, $\hat{A}$ and $\hat{B}$, determining the non-linear stress–strain behaviour for $\varepsilon_t \leq \varepsilon_t^{NL}$, remains limited as well since the slopes in Eq. (19), which respectively differ with 11%, 18% and 10% from those in Eq. (17).

Parameters $\hat{\mathcal{E}}_{NL}$ and ε_t^{NL} determining the linear high-strain behaviour are plotted in Fig. 9. From Fig. 9(b) it is seen that the ratio between the estimated high-strain and low-strain Young's moduli $\hat{\mathcal{E}}_{NL}/\mathcal{E}_{(eff)}$ is mostly smaller than 5 for $\varepsilon_t^{NL} < 0.77$ and smaller than 7 for $\varepsilon_t^{NL} < 0.90$, whereas the ratio is greater than 7 for $\varepsilon_t^{NL} \geq 0.90$. This implies, as plotted for $\varepsilon_t^{NL} \geq \{0.40, 0.77, 0.90\}$ in Fig. 9(a), that the slopes characterising the linear fits ($R^2 = 87\%$, $R^2 = 88\%$ and $R^2 = 91\%$) of $\hat{\mathcal{E}}_{NL}(\mathcal{E}_{(eff)})$ increase with ε_t^{NL}. For $\varepsilon_t^{NL} \geq 0.9$, the resulting slope of 8.55 ($\hat{\mathcal{E}}_{NL} = 8.55\,\mathcal{E}_{(eff)}$) is within 1% of the slope of 8.58 (left border of the shaded region in Fig. 9(a)) found as the solution of Eq. (12) (see Fig. 4). This suggests that although augmenting the number of parameters increases the best fit accuracy, high-strain linear behaviour is only retrieved for $\varepsilon_t^{NL} \geq 0.9$ in which case the high-strain Young's modulus is about 8.55 times the low-strain Young's modulus. From Fig. 9(c) it is seen that the onset of the high-strain region is approximated as a linear fit ($R^2 = 96\%$) of $\max(\varepsilon_t)$, namely $\varepsilon_t^{NL} \approx 0.82\ \max(\varepsilon_t)$, with $\max(\varepsilon_t) \leq 1.36$ for the assessed data sets.

An overview of the overall fit accuracies with different parameter sets for the non-linear exponential and cubic relationships in the range $\varepsilon_t < \varepsilon_t^{NL}$ and a high-strain linear range for $\varepsilon_t \geq \varepsilon_t^{NL}$ is given in Table 4 where the mean and standard deviation of R^2 are reported. Comparing these values with those in Table 3 shows that fit accuracies are similar are either similar or deteriorate. Consequently, accounting for a linear high-strain range does not significantly improve the fit accuracy. Note that without explicitly accounting for a high-strain linear range $\hat{\mathcal{E}}_{NL}$ can still be estimated as $\hat{\mathcal{E}}_{max}$ denoting the slope of the stress–strain curves near $\max(\varepsilon_t)$ since a linear high-strain region implies a constant slope for $\varepsilon_t \geq \varepsilon_t^{NL}$. This is illustrated in Fig. 10 where the relative difference $\Delta\hat{\mathcal{E}}_{NL}$ (in percentage) between $\hat{\mathcal{E}}_{max}$ and $\mathcal{E}_{NL}$ is plotted for $\max(\varepsilon_t) \geq \{0.4, 0.77, 0.9\}$. It is seen that the mean (7.2%, 3.4% and 0.8%) and standard deviation (12.3%, 8.3% and 7.9%) of $\Delta\hat{\mathcal{E}}_{NL}$ decreases for increasing $\max(\varepsilon_t)$. This supports the observation that a linear high-strain range does only occur for $\varepsilon_t^{NL} \geq 0.9$ and thus requires $\max(\varepsilon_t) > 0.9$.

5. Conclusion

In agreement with polynomial and exponential stress–strain relationships for soft biological tissues, best fits (in terms of root mean square error) of two-parameter cubic and exponential relationships are shown to provide an accurate ($R^2 > 99.5\%$) and continuous description of measured low-strain (up to ≈0.3) and subsequent non-linear stress–strain behaviour of ML silicone composite specimens. These composites are characterised by their layer stacking (serial, parallel, combined or arbitrary), measured effective low-strain Young's modulus $\mathcal{E}_{(eff)}$ up to 40 kPa, and some contain a stiff ($\mathcal{E} = 298$ kPa) inclusion as observed in certain structural vocal fold pathologies.

The best fit parameters, minimising the root mean square error between the fitted and measured data (mean fit accuracy $R^2 \geq 99.8\%$), can be approximated as a constant or linear function of $\mathcal{E}_{(eff)}$ with a very limited accuracy loss regardless of the assessed maximum strain as the mean fit accuracy yields $R^2 \geq 97\%$ and $R^2 \geq 94\%$ when respectively the measured or modelled $\mathcal{E}_{(eff)}$ is considered. Besides, the best fit

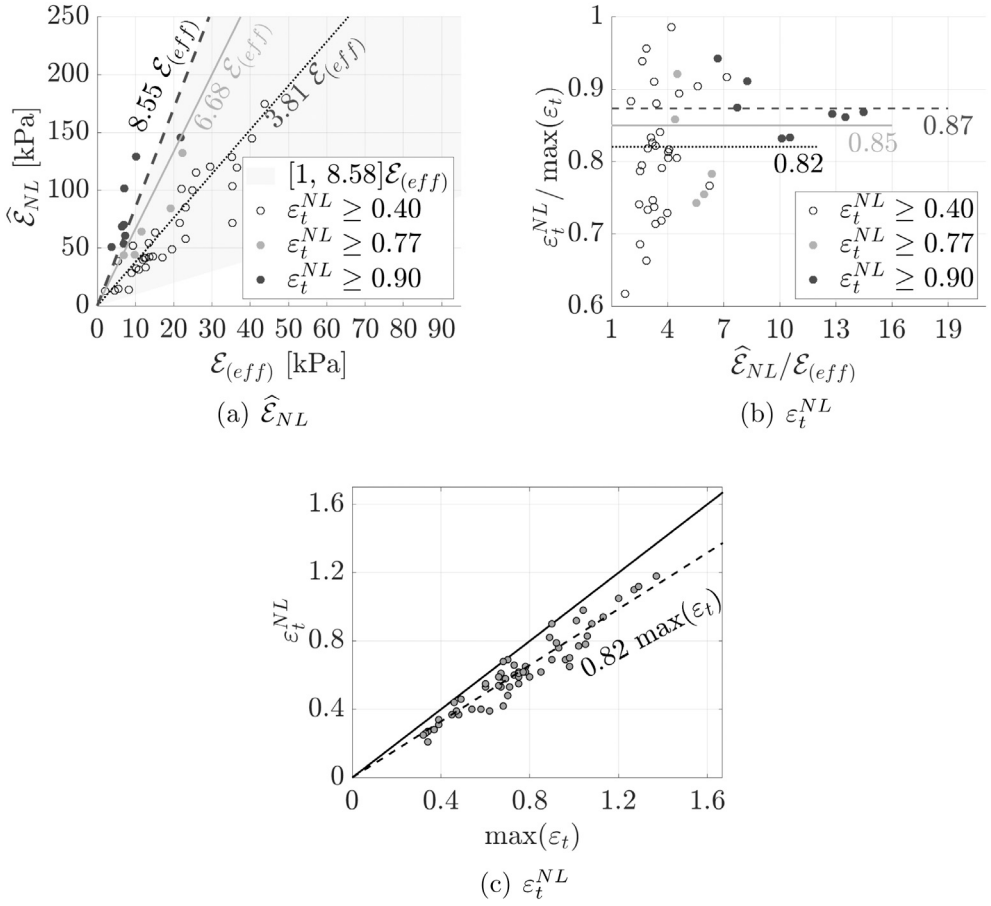

Fig. 9. Linear high-strain elastic parameters ($\widehat{\mathcal{E}}_{NL}$, ε_t^{NL}) for $\varepsilon_t^{NL} \geq \{0.40, 0.77, 0.90\}$: (a) estimated high-strain Young's modulus $\widehat{\mathcal{E}}_{NL}$ as a function of low-strain Young's modulus $\mathcal{E}_{(eff)}$ with shaded region $[1, 8.58]\,\mathcal{E}_{(eff)}$, linear fits ($R^2$ = 87%, R^2 = 88% and R^2 = 91%) are indicated (lines), (b) normalised high-strain lower limit $\varepsilon_t^{NL}/\max(\varepsilon_t)$ as a function of the ratio between high-strain and low-strain Young's moduli $\widehat{\mathcal{E}}_{NL}/\mathcal{E}_{(eff)}$, mean values (horizontal lines) are indicated (standard deviation of 10%, 7% and 4%), (c) ε_t^{NL} as a function of $\max(\varepsilon_t)$, linear fit (dashed line) (R^2 = 96%) and identity function (full line).

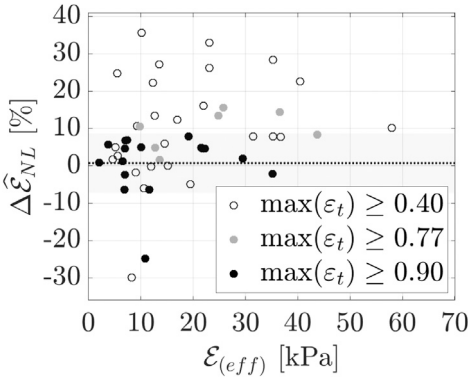

Fig. 10. Relative difference $\Delta\widehat{\mathcal{E}}_{NL}$ between the linear stress–strain slope $\widehat{\mathcal{E}}_{max}$ estimated near $\max(\varepsilon_t)$ and $\mathcal{E}_{NL}$ near ε_t^{NL} for $\max(\varepsilon_t) \geq \{0.4, 0.77, 0.9\}$. The shaded region indicates the mean (0.8%, dotted line) plus and minus the standard deviation for $\max(\varepsilon_t) \geq 0.9$.

parameters and their approximations, *a priori* modelled parameter sets are derived as well. These modelled parameters depend on $\mathcal{E}_{(eff)}$ in the same way as the approximated best fit parameters. Contrary to the best fit parameter sets and subsequent approximated best fit parameters, no data are used to derive the modelled parameter sets so that the found accuracy (mean fit accuracy $R^2 \geq 85\%$ with measured or modelled $\mathcal{E}_{(eff)}$) supports the model approach which uses the assumption that the cubic and exponential relationship match at a strain-value corresponding to at least 64% of the maximum strain. This ensures that both relationships as well as their strain energy density functions agree to within 12.6% for the full strain range. Thus for a matching strain value of 1.0, the cubic and exponential relationships, and hence the modelled two-parameter sets, can be applied for strains up to 1.55, which is about 4.5 times the low-strain limit. In addition, a modelled expression for the high-strain elastic Young's modulus $\mathcal{E}_{NL}$, characterising a linear high-strain stress behaviour, is obtained as $8.58\,\mathcal{E}_{(eff)}$. Consequently, both approximated best fit parameters and *a priori* modelled parameters can be used to characterise the linear and non-linear stress–strain relationship once $\mathcal{E}_{(eff)}$ is known, where $\mathcal{E}_{(eff)}$ is either measured or modelled. Therefore, combining the previously proposed low-strain Young's modulus model (Ahmad et al., 2021, 2022) with the cubic or exponential stress–strain characterisation and approximated or modelled two-parameter sets as a function of $\mathcal{E}_{(eff)}$ results in an *a priori* stress–strain characterisation. This is of particular benefit for the design of ML silicone composites and thus in term for the design of vocal fold replicas which so far relied on a tedious and *a posteriori* experimental characterisation. It is of interest to further investigate stress–strain curves with strains up to 1.55 or more in order to further confirm the linear high-strain behaviour. In addition, the proposed modelled non-linear two-parameter relationships, with *a priori* modelled parameter, can be compared with other hyperelastic multi-parameter constitutive laws requiring a more extensive data based fitting.

CRediT authorship contribution statement

Mohammad Ahmad: Writing – original draft, Investigation, Data curation, Conceptualization. **Xavier Pelorson:** Supervision, Methodology. **Oriol Guasch:** Writing – original draft, Funding acquisition. **Ana Inés Fernández:** Writing – original draft, Methodology, Funding acquisition. **Annemie Van Hirtum:** Writing – original draft, Supervision, Methodology, Funding acquisition, Formal analysis, Conceptualization.

Declaration of competing interest

The authors declare that they have no known competing financial interests or personal relationships that could have appeared to influence the work reported in this paper.

Data availability

Data will be made available on request.

Acknowledgements

This work was partly supported by the Full3DTalkingHead project (ANR-20-CE23-0008-03) and a PhD grant from the French Ministry of Education and Research. O. Guasch acknowledges the funding of the Agencia Estatal de Investigación (AEI) through the FEMVoQ project (PID2020-120441GB-I00/AEI/10.13039/501100011033). A.I. Fernández thanks the Catalan Government for the quality accreditation of her research group (DIOPMA 2017 SGR 0118).

References

Ahmad, M., Bouvet, A., Pelorson, X., Va. Hirtum, A., 2021. Modelling and validation of the elasticity parameters of multi-layer specimens pertinent to silicone vocal fold replicas. Int. J. Mech. Sci. 208, 106685.

Ahmad, M., Pelorson, X., Fernández, I., Guasch, O., Van Hirtum, A., 2022. Low-strain effective Young's modulus model and validation for multi-layer vocal fold based silicone specimens with inclusions. J. Appl. Phys. 131, 1–12.

Alipour, F., Titze, I., 1991. Elastic models of vocal fold tissues. J. Acoust. Soc. Am. 90, 1326–1331.

Alipour, F., Vigmostad, S., 2012. Measurement of vocal folds elastic properties for continuous modeling. J. Voice 26, 816e21–816e29.

Bouvet, A., 2019. Experimental and Theoretical Contribution to the Analysis and the Modelling of the Vocal Folds Vibration (Ph.D. thesis). Grenoble Alpes University, France.

Bouvet, A., Pelorson, X., Van Hirtum, A., 2020b. Influence of water spraying on an oscillating channel. J. Fluids Struct. 93, 1–20.

Bouvet, A., Tokuda, I., Pelorson, X., Van Hirtum, A., 2020a. Influence of level difference due to vocal folds angular asymmetry on auto-oscillating replicas. J. Acoust. Soc. Am. 147, 1136–1145.

Burks, G., De Vita, R., Leonessa, A., 2020. Characterization of the continuous elastic parameters of porcine vocal folds. J. Voice 34.

Chan, R., Fu, M., Young, L., Tirunagari, N., 2007. Relative contributions of collagen and elastin to elasticity of the vocal fold under tension. Ann. Biomed. Eng. 35, 1471–1483.

Chhetri, D., Zhang, Z., Neubauer, J., 2011. Measurement of Young's modulus of vocal folds by indentation. J. Voice 25, 1–7.

Demiray, H., 1972. A note on the elasticity of soft biological tissues. J. Biomech. 5, 309–311.

Drechsel, J., Thomson, S., 2008. Influence of supraglottal structures on the glottal jet exiting a two-layer synthetic, self-oscillating vocal fold model. J. Acoust. Soc. Am. 123, 4434–4445.

Friedrich, G., Dikkers, F.G., Arens, C., Remacle, M., Hess, M., Giovanni, A., Duflo, S., Hantzakos, A., Bachy, V., Gugatschka, M., 2013. Vocal fold scars: Current concepts and future directions, consensus report of the Phonosurgery Committee of the European Laryngological Society. Eur. Arch. Otorhinolaryngol. 270, 2491–2507.

Fung, Y., 1967. Elasticity of soft tissues in simple elongation. Am. J. Physiol. 213, 1605–1624.

Fung, Y., 2010. Biomechanics. Springer.

Hansen, J.K., Thibeault, S.L., 2006. Current understanding and review of the literature: Vocal fold scarring. J. Voice 20, 110–120.

Hirano, M., Kurita, S., Nakashima, T., 1983. Vocal Fold Physiology: Contempory Research and Clinical Issues. College-Hill Press, pp. 22–43.

Mattei, A., Magalon, J., Bertrand, B., Philandrianos, C., Véran, J., Giovanni, A., 2017. Cell therapy and scarred vocal folds. Eur. Ann. Otorhinolaryngol. Head Neck Dis. 134, 339–349.

Min, Y., Titze, I., Alipour, F., 1995. Stress-strain response of the human vocal ligament. Ann. Otol. Rhinol. Laryngol. 104, 563–569.

Miri, A., 2014. Mechanical characterization of vocal fold tissue: A review study. J. Voice 28, 657–666.

Murray, P., Thomson, S., 2012. Vibratory responses of synthetic, self-oscillating vocal fold models. J. Acoust. Soc. Am. 132, 3428–3438.

Pickup, B., Thomson, S., 2010. Flow-induced vibratory response of idealized versus magnetic resonance imaging-based synthetic vocal fold models. J. Acoust. Soc. Am. 128, 124–129.

Reuss, A., 1929. Berechnung der fließgrenze von mischkristallen auf grund der plastizitätsbedingung für einkristalle. ZAMM Z. Angew. Math. Mech. 9, 49–58.

Riede, T., Tokuda, I., Munger, J., Thomson, S., 2008. Mammalian laryngseal air sacs add variability to the vocal tract impedance: Physical and computational modeling. J. Acoust. Soc. Am. 124, 634–647.

Rosen, C., Simpson, C., 2008. Operative Techniques in Laryngology. Springer-Verlag.

Smith, S., Thomson, S., 2012. Effect of inferior surface angle on the self-oscillation of a computational vocal fold model. J. Acoust. Soc. Am. 131, 4062–4075.

Tanaka, M., Weisenbach, C., Miller, M., Kuxhaus, L., 2011. A continuous method to compute model parameters for soft biological materials. J. Biomech. Eng. 133, 1–7.

Voigt, W., 1889. Ueber die beziehung zwischen den beiden elasticitätsconstanten isotroper körper. Ann. Phys. 274, 573–587.

Zhang, Z., Drapaca, C., Chen, X., Xu, J., 2017. Droplet squeezing through a narrow constriction: Minimum impulse and critical velocity. Phys. Fluids 29, 1–9.

Zhang, K., Siegmund, T., Chan, R., 2006. A constitutive model of the human vocal fold cover for fundamental frequency regulation. J. Acoust. Soc. Am. 119, 1050–1062.